Open Ceramics 2 (2020) 100019

Contents lists available at ScienceDirect

Open Ceramics

journal homepage: www.editorialmanager.com/oceram

Roadmap for densification in cold sintering: Chemical pathways

Arnaud Ndayishimiye [a,b,*], Mert Y. Sengul [a,b], Takao Sada [a,c], Sinan Dursun [a,b], Sun Hwi Bang [a,b], Zane A. Grady [a,b], Kosuke Tsuji [a,b], Shuichi Funahashi [d], Adri C.T. van Duin [a,e], Clive A. Randall [a,b]

[a] Materials Research Institute, The Pennsylvania State University, University Park, PA, 16802, United States
[b] Department of Materials Science and Engineering, The Pennsylvania State University, University Park, PA, 16802, United States
[c] Monozukuri R&D Laboratory, KYOCERA Corporation, Kirishima, Kagoshima, 899-4312, Japan
[d] Murata Manufacturing Co., Ltd., 1–10–1 Higashikotari, Nagaokakyo, Kyoto, 617–8555, Japan
[e] Department of Mechanical Engineering, The Pennsylvania State University, University Park, PA, 16802, United States

ARTICLE INFO

Keywords:
Cold sintering
Pressure solution
ReaxFF
Molecular dynamics
Ceramics

ABSTRACT

The cold sintering process (CSP) is a technique that enables densification of ceramics and composites at extremely low temperatures (T < 400 °C) with the application of a uniaxial pressure and a transient solvent. At the laboratory scale, comparing direct sintering methods relative to CSP evidences that the latter could enable a sustainable eco-manufacturing path with considerable energy and emission savings, as well as fast processing times. Thus far, cold sintering has been applied to different materials, compounds, solid solutions, and functional composites, pointing to multiple future opportunities. This paper summarizes some of the transient phase selections, different chemical approaches and subtle chemical reactions with the powders which can be used to drive the cold sintering processes in many important ceramics and composites. In doing so, this paper highlights some of the reasons why the fundamental understanding of CSP mechanisms remains challenging, but classification of the pathways as outlined here should aid progress towards a more comprehensive understanding.

1. Introduction

The use of solvents and uniaxial pressure to densify inorganic materials was first demonstrated by Della M. Roy et al. in the early 1970's to fabricate cement pastes with excellent mechanical properties. Heat and pressure were used to control the porosity and accommodate volume changes occurring during the cement hydration [1,2]. Within the same decade, advances in hydrothermal processing were carried out by S. Sōmiya et al. to densify oxides through a reactive approach from metal powders at temperatures below 1000 °C [3,4]. In the 1980's, N. Yamasaki, K. Yanagisawa et al. developed an apparatus for "hydrothermal hot pressing" combining the two previous approaches, based on the uniaxial pressure of a mixture of powder and an aqueous solutions in a system sealed with PTFE (Teflon™) gaskets [5]. This technique led to the sintering of several oxides through a dissolution-precipitation mechanism, as stated by authors [6–10]. As the technique was limited in terms of relative densities achieved, a high-performance "solvo-/hydrothermal sintering" apparatus was designed by Goglio et al. to reach higher temperatures and pressures without damaging the Teflon™ gaskets while maintaining the hermetic sealing of the system [11,12]. These improvements led to the fabrication of high density SiO_2, SiO_2-based composites [13–15] and metal composites [16] through mecha nical-chemical effects in synergy with chemical effects [12,13]. Riman et al. developed the " Reactive Hydrothermal Liquid Phase Densification" (rHLPD) for the reactive crystallization and densification of materials [17]. In this process, a porous preform is infiltrated with precursors then exposed to mild isostatic pressures and temperatures to drive hydrothermal reactions between the preform and precursors [18,19].

There is now growing interest in the cold sintering process (CSP) [20,21], a low temperature and energy efficient [22] sintering technique based on the uniaxial pressure of a powder mixed with a solvent in the presence of moderate heat. The densification is mainly driven by a pressure solution creep mechanism [23–25]. So far, several approaches have been used to cold sinter at least a hundred of ceramics and composites in both bulk form and with a multilayer structure [26–29]. The successful densification of these materials in a single step at temperatures which are a fraction of the conventional sintering temperature is contingent on the proper selection of transient phase chemistry. There

* Corresponding author. Materials Research Institute, The Pennsylvania State University, University Park, PA, 16802, United States.
E-mail address: axn536@psu.edu (A. Ndayishimiye).

https://doi.org/10.1016/j.oceram.2020.100019
Received 13 July 2020; Accepted 20 August 2020
Available online 26 August 2020

are limited experimental resources and instrumentation available to predict or enable *in situ* investigations of chemical reactions within the cold sintering processing conditions. Despite such limitations, the role of chemistry in cold sintering has become undeniably apparent in both solvent selection and the proposed CSP mechanisms. In this paper, we summarize the main pathways and chemical insights that have been used to cold sinter most of the ceramics and composites. Based on several experimental investigation of distinct materials systems, we highlight the current understanding of CSP, as well as limitations and challenges that still need to be addressed.

2. General considerations for CSP

2.1. Cold sintering protocols

For each sample a powder and a transient liquid were manually mixed with an agate mortar and pestle for 2–5 min. The mixture was then poured into a 12.6 or 13 mm diameter stainless steel die and uniaxially pressed using a Carver Model M press or a device composed of a) an ENERPAC press able to automatically maintain the pressure constant with the help of an electric hydraulic pump, b) a dilatometer with a Keyence GT2-H32 Digital Contact Sensor [30]. The mixture was first pressed under the sintering pressure at room temperature for 10 min to allow further particle rearrangement [31], then the temperature was increased to the sintering temperature with a 20 °C min^{-1} average heating rate. The mixture was then maintained in the die at sintering temperature for a certain time and the pressure was manually or automatically readjusted when shrinkage was observed. The sintering conditions of materials presented in this paper are summarized in Supplementary Data, Table S1.

2.2. Cold sintering mechanisms

2.2.1. Mechano-chemical effects

Densification with CSP is mainly based on pressure solution mechanism, often encountered in geoscience [25,32]. This mechanism is driven by chemical potential gradients from highly constrained areas with enhanced dissolution and high chemical potential to low constrained areas at particle surfaces with a lower chemical potential, through atomically thin liquid film at the contacting particle surfaces. A discussion of the thermodynamic principles governing pressure solution in cold sintering is made in section II.2.3. The pressure solution is conceptually similar to Coble and Nabarro-Herring creep laws which are driven by grain boundary and intragranular diffusion, respectively [25,32]. However, pressure solution creep occurs at much lower temperatures than these two other mechanisms owing to the diminished activation energy of diffusion lower in liquids and at surfaces relative to bulk diffusion in solids.

2.2.2. Chemical effects

Dynamic chemical interactions between the liquid solvent and the surface of the inorganic materials drives dissolution and can be enabled in variety of ways including chelating, dehydration and cluster formation reactions. It is difficult to observe or predict the details of these nonequilibrium interactions experimentally, but the reactive force field (ReaxFF) molecular dynamics technique has proven very useful in gaining theoretical insight into these dynamic interactions [33–35]. The observation of highly defective grain boundaries, which reduce the activation energy for atomic diffusion by Gonzalez-Julian et al. [36] and the formation of bonds between adjacent particles by Shen [37] and Goglio et al. [13] have also been reported as evidence for the procession of the aforementioned chemical effects occurring during CSP.

2.2.3. Challenges in the fundamental investigation of CSP

Pressure solution creep has been recognized as a rock deformation mechanism in the geologic literature since its introduction by Henry B. Sorby in the 1860's [38]. Despite knowledge of the major steps characterizing pressure solution creep and observations of this mechanism in geologic studies, details of it thermodynamics and kinetics are not yet fully understood and have been intensively debated for over a century by geologists, and largely ignored in the field of material science [39]. A detailed discussion of the contending explanations of pressure solution creep is beyond the scope of this paper, but interested readers should refer to a recent comprehensive historical review of the process by Gratier et al. [25] (specifically, section 3.4.). In CSP, the pressure solution creep mechanism occurs due to the application of uniaxial pressure upon a solid in the presence of a fluid in an open system. The process is thus governed by the non-equilibrium thermodynamics of locally-controlled solid-fluid interface-coupled dissolution-precipitation mechanisms within confined spaces; but also by the thermodynamics of non-hydrostatically stressed solids, as defined by the Gibbs-Kamb theory [40]. Shimizu showed that hydrostatic pressure does not affect the entire process of dissolution-mass transport-precipitation, therefore excluding it from possible causes of pressure solution creep [39]. The driving force of pressure solution creep is thus not "pressure" [41], but rather the stress gradients in the solids, manifested by the difference in chemical potentials across solid-fluid boundaries [39]. The application of the aforementioned non-equilibrium thermodynamic principles applied to open systems remains a largely open question, so the extension of such principles in the search of a fundamental understanding of CSP is similarly unresolved. There are also experimental challenges to fundamentally investigate CSP as there is a lack of *in situ* characterization techniques that can operate under the applied processing conditions. For example, it is only recently that localized solid-fluid interface-coupled dissolution-precipitation reactions have been monitored *in situ* using atomic force microscopy (AFM) [42,43]. To extend such techniques to CSP, instruments would need to be developed to allow for such measurements under a load with an evaporating solvent.

2.2.4. Contrast with Kingery's pressure-assisted sintering in the presence of a liquid phase

As previously stated, pressure solution creep is conceptually similar to Coble and Nabarro-Herring creep laws but occurs at lower temperatures due to the presence of a liquid phase. Kingery et al. [44] studied the effects of applied pressure on densification during sintering in the presence of a liquid phase on a macroscopic scale. The main mechanism described for this type of system is the solution-precipitation, with the rate of densification given by Equation (1):

$$\frac{\Delta l}{l_0} = \frac{1}{3}\frac{\Delta v}{v_0} = \left[\frac{3\, k_2 \delta\, D_L C_0 V_0}{r^3 RT}\left(\frac{2\gamma_{lv}}{k_1 r} + P\right)\right]^{1/3} t^{1/3} \quad (1)$$

where $\Delta l/l_0$: time-dependent fractional linear shrinkage (often called strain (ε) in several references), $\Delta v/v_0$: fractional volume shrinkage, k_1 and k_2 are geometrical constants, δ: thickness of liquid film between solid grains, D_L: diffusion coefficient in liquid, C_0: solubility of solid in liquid, V_0: molar volume of dissolving material, γ_{lv} : liquid-vapor surface energy, r: initial particle radius, R: gas constant, T: absolute temperature and P: applied pressure.

Based on experimental measurements, Kingery et al. [44] have shown that the applied pressure in the presence of a liquid phase could be effective by increasing the extent and rate of particle rearrangement, increasing the rate of dissolution of solution at points of particle contact, and causing plastic flow within solid particles.

Kingery's model does not explicitly build upon the thermodynamic models previously discussed and therefore cannot be confidently used for pressure solution creep-driven systems. In order to describe macroscopic deformation occurring during the pressure solution creep of quartz in the presence of water, Shimizu used chemical potentials defined by non-hydrostatic and non-equilibrium thermodynamics to estimate the strain rate ($\dot{\varepsilon}$) during the process [39]. Two distinct scenarios were distinguished: (a) the diffusion coefficient in the water film between two grains

is small. Two distinct scenarios were distinguished: (a) the diffusion coefficient in the water film between two grains is small. In this case, pressure solution creep is diffusion-controlled, as the strain rate is inversely proportional to d^3 (Equation (2)), where d is the diameter of the grains and (b) the diffusion coefficient in the water film is large, in which case the pressure solution creep process is reaction-controlled and the strain rate is inversely proportional to d (Equation (3)).

$$\dot{\varepsilon} = \frac{\alpha \nu_{SiO_2}^2 K D w}{\nu_{H_2O} R T d^3} \sigma \quad (2)$$

$$\dot{\varepsilon} = \frac{\beta \nu_{SiO_2}^2 k_+}{\nu_{H_2O} R T d} \sigma \quad (3)$$

where α: shape factor ($\alpha \approx 16$) depending on grain shape and grain distribution, β : shape factor depending on the roughness of the interface ($\beta \approx 2$ for a smooth and $\beta > 2$ for a rough interface), ν : molar volume, D: grain boundary diffusion coefficient, d: diameter of grains, w : grain boundary width, K: equilibrium constant, k_+ : rate constant of dissolution, R: gas constant, T: absolute temperature and σ: deviatoric stress.

The nature of chemical interactions at these interfaces, with temperature, local stress gradients, and particle sizes then have a direct impact on the dissolution rate equations. Strain rates during pressure solution evolve with the grain boundary width, in relation with the evolutive amount of solvent at grain boundaries during the process. High strain rates, showing rapid pressure solution, are observed in early stages when w is high.

2.2.5. Pathways towards densification

Different pathways towards single step densification using cold sintering are summarized in Fig. 1. The "material" parameters are determined by physico-chemical characteristics of the initial powder such as the chemical composition including surface chemistry, crystal structure, particle size, and their particle size distribution. Solvent selection is a critical step to successfully perform single step densification of materials by cold sintering. In applying cold sintering to a variety of material systems, empirically-chosen solvents ranging from aqueous, low boiling point non-aqueous, and low melting temperature molten hydroxides/salts have been employed, based on general chemical solubility principles. The proper solvent enables chemical interactions with the powder under appropriate processing conditions (heating and cooling ramp rates, temperature, pressure, and dwell time) which then activates the densification. Depending on the chemistry of the particle-solvent interaction, either congruent or incongruent dissolution of the surface can occur:

- Congruent dissolution: Cold sintering proceeds unabated, as the material dissolves into the solvent with a homogeneous chemical stoichiometry prior to mass transport and precipitation.
- Incongruent dissolution: Cold sintering is impeded as ions with higher dissolution kinetics are leached out before ions with slower dissolution kinetics. As a result, particle surfaces become passivated which separates the solvent and the crystalline phase, often hindering densification. The degree and nature of the barriers to CSP under incongruently dissolving conditions may depend on a number of factors such as type of anionic ligands, crystal structures of the solid surface, and bond energies. One of the strategies used to address incongruent dissolution is the use of a solvent saturated with the same ions which are preferentially leached [45]. This reduces the kinetics of dissolution of the preferentially leached ion into the solution, while not greatly affecting the dissolution of the other constituent ions, thus mitigating the surface passivation process and allowing CSP to proceed.

In one of the initial studies of cold sintering, Guo et al. [26] observed amorphous/glassy phases precipitated at grain boundaries following a rapid evaporation, kinetically limiting the crystallization. In such cases these amorphous/glassy phases could be crystallized by using an annealing step. It has been recently shown that annealing can be avoided by the use of more chemically active solvents, such as molten hydroxides and salts [46–48].

3. Chemical pathways in CSP

Here, the different experimentally-observed scenarios which result in dense compounds by CSP are classified and summarized. These scenarios can be applied to both binary and multi-element compounds [27]. Solvent selection is a determining step as it activates cold sintering mechanisms and therefore densification at low temperatures, thanks to chemical reactivity.

3.1. Choice of solvent

As described in a provisional CSP patent [49], several solvents such as organic alcohols, ketones, esters, water and/or mixtures can be used to

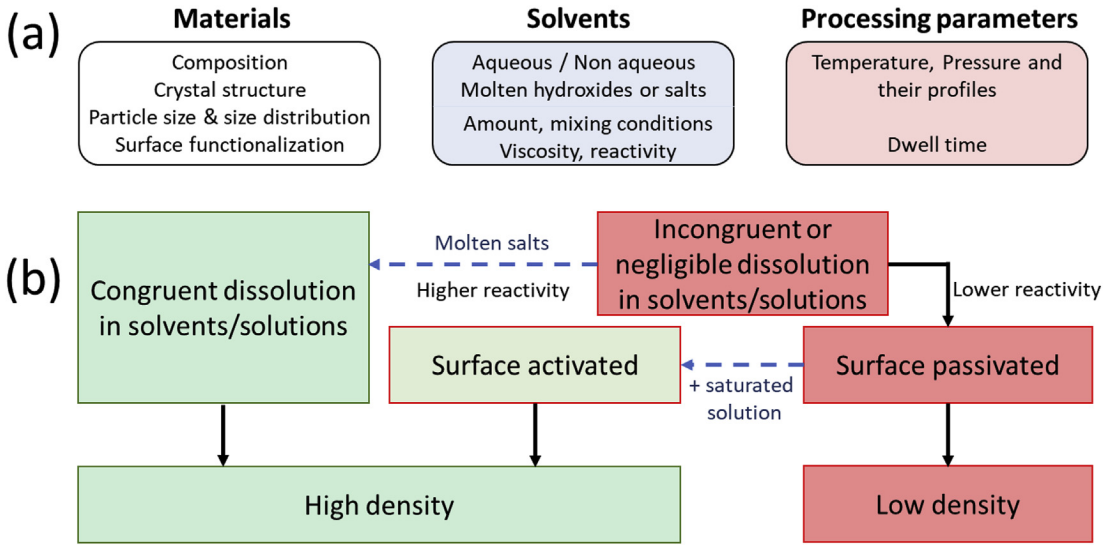

Fig. 1. Schematic diagram showing (a) the key parameters to be considered for cold sintering and (b) the different pathways necessary to optimize a single step densification with cold sintering upon the nature of the dissolution step.

densify materials at low temperature. The pH of an aqueous solvent may be modified by the introduction of additives to promote the dissolution of the target compound. Several polar ($\varepsilon' > 50$) and semi-polar solvents ($20 > \varepsilon' > 50$) (Fig. 2) have been employed in cold sintering as a high relative permittivity of the liquid phase promotes the dissolution of inorganic compounds. The boiling point of the solvent should also be considered, as this property must be within the attainable temperature window of the cold sintering apparatus.

Other types of solvents such as deep eutectic solvents [50–52], molten salts and hydroxides [53], in which many oxides and refractory metals are soluble, can also be used. These solvents do not boil off, but rather melt during cold sintering and are expelled as the material densifies due to the open nature of the process. Funahashi et al. [54] recently demonstrated that chelating agents in the form of metal-acetylacetonates can be used in CSP of spinels.

3.2. Different chemical pathways

In cold sintering, there are diverse pathways to obtain dense materials (Fig. 3). In the first pathway, which is the most commonly used, a compound **A** leads to the same compound **A** (**A** → **A**) as the initial powder and the final material are of the same composition and crystallographic phase. Alternatively, there is a pathway where a compound **A** leads to a compound **B** (**A** → **B**), where the final material has a different chemical composition or crystallographic phase than the initial powder. Finally, there exists the possibility for **A** + **B** → **C**, which is a reactive route, where a mixture of compounds **A** and **B** can whether lead to a chemical doping or to a new compound after CSP.

3.2.1. Pathway A → A

To date, cold sintering following pathway A → A has been most commonly demonstrated. The initial powder has the same chemical composition and crystallographic phase as the densified material. Here, we show examples of single step densification of various ceramics as well as templated grain growth with a CSP step.

3.2.1.1. Single step densification. Single step densification of ceramics at low temperature is possible when the appropriate transient liquid and optimum sintering conditions are selected. Here, examples of the densification of several materials systems such as ZnO, $BaTiO_3$, Fe_3O_4 or ferrites using different solvents are described in order to provide insight into the chemical approaches used for solvent selection.

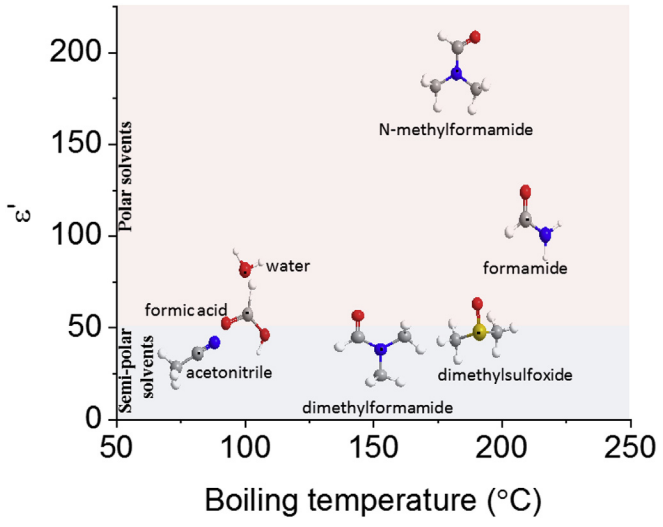

Fig. 2. Selected examples of polar and semi-polar solvents used in cold in cold sintering, with their relative permittivity (ε′) and boiling temperature.

- **Zinc oxide (ZnO)** is mainly known as a n-type semiconductor with high electron mobility, thermal conductivity and controllable electrical conductivity [55]. The CSP of ZnO with acetic acid aqueous solutions or with a liquid comprised of dissolved zinc acetate [56] have been extensively studied after the first demonstration by Funahashi et al. [57] The chemical effects driving densification in this system were studied by Sengul et al. [33–35], using ReaxFF, a reactive molecular dynamics method, as there are currently no equipment available for their thorough experimental *in situ* investigation.

Here, we show the difference between CSP of ZnO using two different transient liquids: water and an acetic acid aqueous solution. In CSP conditions, interactions between acetic acid and a ZnO surface lead to dynamic chelating reactions to form zinc acetate hydrate species (Fig. 4c) at particle/particle contact points during dissolution. Dissolved species are transported as a result of chemical potential gradients in the system, then precipitate and crystallize in less stressed surfaces after being decomposed during dynamic ZnO surface/acetate interactions. At a molecular level, the decomposition reaction starts with a nucleophilic attack of oxygen to methyl carbon, resulting in the formation of carbon dioxide (CO_2) and formaldehyde (CH_2OH) molecules [33]. When water is used as a transient liquid, ReaxFF molecular dynamic simulations highlight that $Zn^{2+} \cdot 4H_2O$ and $Zn(OH)_2 \cdot 2H_2O$ species are formed in CSP conditions (Fig. 4a–b), from first and second-order hydrolysis reactions [58], respectively. Although these species may decompose more easily compared to acetates upon interaction with the ZnO surfaces, it was recently shown by Bang et al. that linear shrinkage in the ZnO/water system is less important than in the ZnO/2 M acetic acid system (Fig. 4d) [59] and does not lead to densification [57]. At constant size, ZnO particles have a lower solubility in pure water than in acetic acid. As a result, there is a low concentration of species available to effectively drive densification *via* a pressure solution mechanism. This shows the importance of both the concentration of species obtained during the dissolution step and their nature, which have a major influence on their ability to decompose, precipitate and recrystallize on oxide surfaces.

- **Barium titanate ($BaTiO_3$)**, a high permittivity dielectric widely used to fabricate capacitors has been extensively investigated by cold sintering [23,45]. Early investigations on the CSP of $BaTiO_3$ have shown that the use of water, aqueous solutions or suspensions result in a ceramic that requires annealing at high temperatures (700–900 °C) to have both a high relative density and high performance dielectric properties. Guo et al. reasoned that the necessity of an annealing step was as a consequence of the presence of a Ba-carbonate amorphous layer at grain boundaries, which lowered the dielectric permittivity of bulk ceramics [23]. Here, different alkali solutions and fluxes are used as examples to highlight important factors to consider for the densification of $BaTiO_3$. In Fig. 5a, we show the CSP of $BaTiO_3$ with a NaOH flux at 240 °C (a $T < T_m$ NaOH ≈ 318 °C, T_m: melting temperature), 240 MPa and 60 min, as well as the dinfluence of water addition on densification (see detailed conditions in Supplementary Data, Figure S 1). In the applied sintering conditions, $BaTiO_3$ has a relative density of 81.4% when no water is added. Alkali hydroxides have a high viscosity below their melting temperature, [60] which can affect the mass transport although the chemical reactivity at interfaces may be high enough to locally dissolve $BaTiO_3$ surface. The addition of small amounts of water, 3 and 5 μL, are shown to be beneficial to densification, as the relative density increases to 82.7 and 85.7%, respectively. This observation allows us to hypothesize that these small amounts of added water are within the range to maintain the chemical reactivity of NaOH to activate the dissolution process at contact points between particles, thus enabling the pressure solution creep mechanism. Furthermore, the viscosity of the transient flux might be decreased, which would therefore increase the diffusion of dissolved species [61].

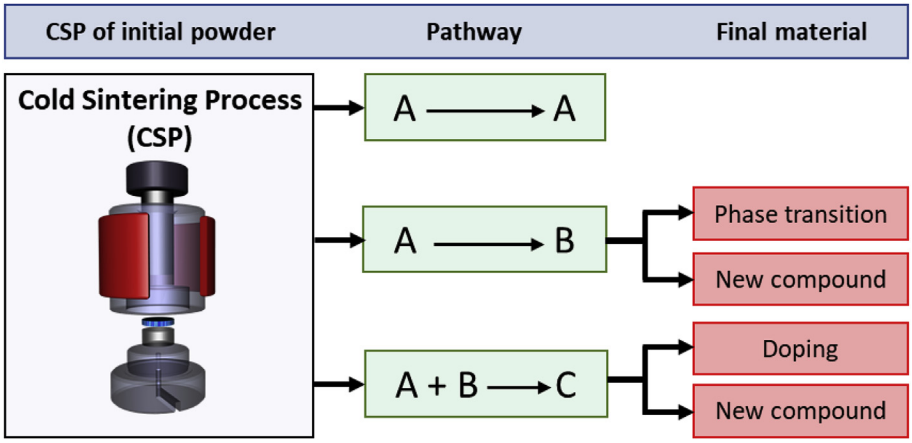

Fig. 3. Different chemical pathways in cold sintering.

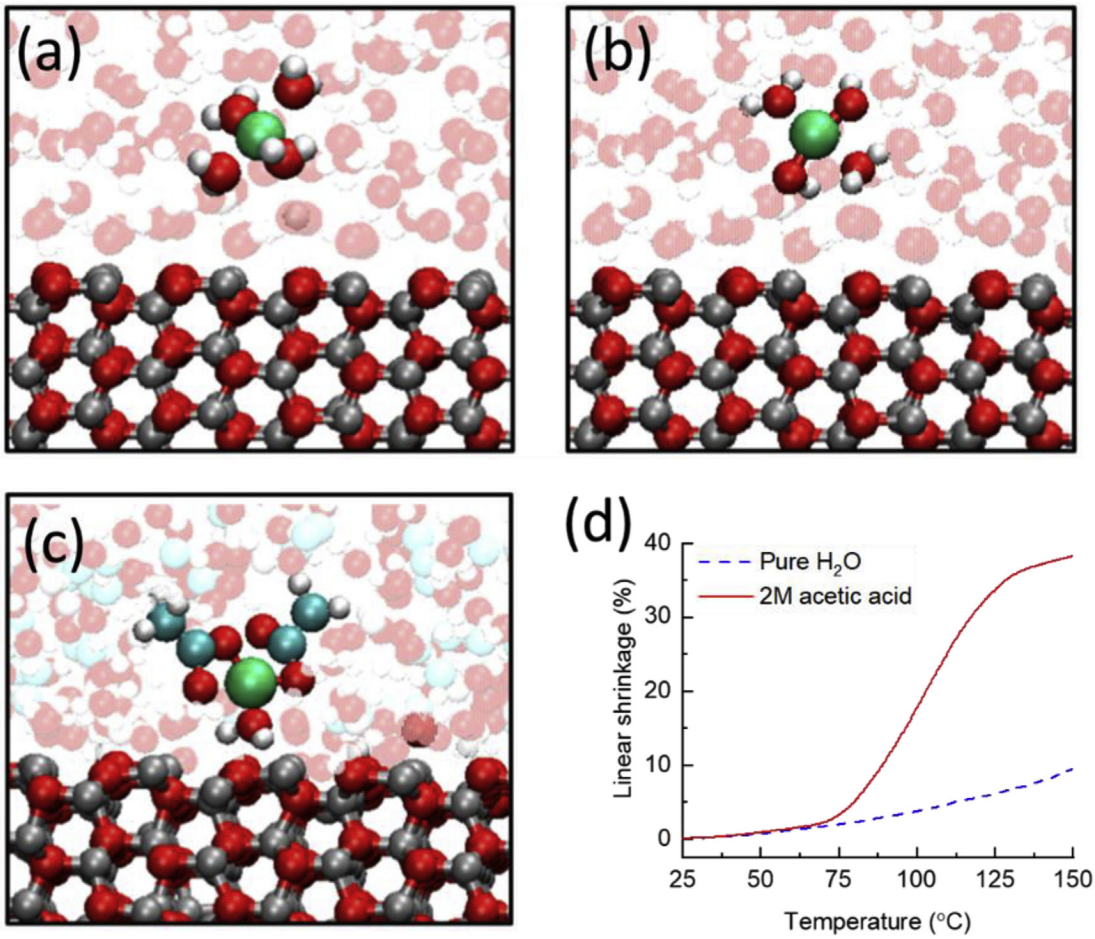

Fig. 4. (a–c) Visualization of ReaxFF simulations that show the Zn^{2+} speciation in solution. The chemical environment of Zn^{2+} can be different depending on the chemical conditions. At the ZnO/water interface, we can observe (a) Zn^{2+} surrounded by four water molecules ($Zn^{2+} \cdot 4H_2O$) and (b) Zn^{2+} ion surrounded by two water molecules and two hydroxides $Zn(OH)_2 \cdot H_2O$. At the ZnO/acetate interface, we can observe (c) Zn^{2+} connected to two acetate ions and one water molecule ($Zn(CH_3CO_2)_2 \cdot H_2O$. Key: Zn^{2+} in solution phase (green); Oxygen (red); Hydrogen (white); Surface Zinc (grey); Carbon (cyan). Background atoms are lighter colored to increase visibility. (d) Linear shrinkage dependence on the transient liquid in the anisothermal regime [59]. (For interpretation of the references to color in this figure legend, the reader is referred to the Web version of this article.)

The addition of more water (>5 μL) in the system leads to a gradual decrease in relative density (Fig. 5a). The chemical reactivity of NaOH in relation to the $BaTiO_3$ surface may be affected by the excess water, therefore less dissolved species are available for mass transport although their diffusion is favored.

To further understand the intrinsic effect of added water in the cold sintering of $BaTiO_3$ when molten alkali fluxes are used as the transient liquid, ReaxFF simulations were conducted on systems composed of $BaTiO_3$ and NaOH–KOH eutectic composition in the presence and absence of added water. The ReaxFF simulations are conducted at a

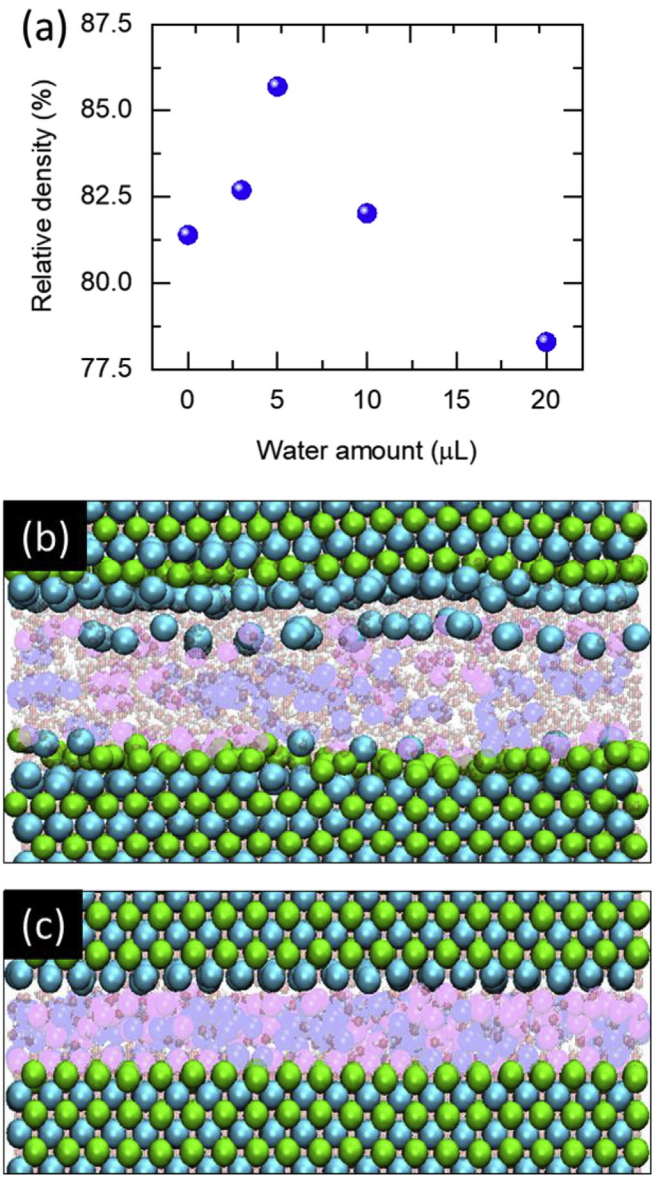

Fig. 5. (a) Influence of the amount of added water on the relative density of $BaTiO_3$ cold sintered at 240 °C, 240 MPa and 60 min with NaOH as a transient liquid. (b) Snapshot for NaOH–KOH aqueous solution and (c) NaOH–KOH eutectic flux obtained as a result of ReaxFF molecular dynamics simulations. Key: Barium (light blue); Titanium (green); Potassium (purple); Sodium (blue); Oxygen atoms (red); Hydrogen atoms (white). Water molecules, potassium and sodium ions that are not of interest are lighter colored. The same colorization is used for all images. (For interpretation of the references to color in this figure legend, the reader is referred to the Web version of this article.)

temperature of 300 °C and a pressure of 500 MPa, and the simulated $BaTiO_3$ interfaces involve TiO_2 and BaO surface terminations (see Supplementary Data, Procedure SP1 for the details of simulations). Our ReaxFF molecular dynamics results demonstrate a difference in dissolution mechanisms between flux conditions with and without added water (Fig. 5b and c). The presence of water in the system resulted in the incongruent dissolution of Ba^{2+} into the solvent phase (Fig. 5b). This behavior was reported before [62] and therefore expected.

However, according to our simulations, such dissolution mechanism is prevented when there is no extensive water in the system (Fig. 5b), which may confirm congruent dissolution assumptions by Tsuji et al. [46] in a similar experimental system. One of the reasons why incongruent dissolution is prevented in the $BaTiO_3$/molten hydroxide system is correlated with interactions of sodium and potassium ions with the $BaTiO_3$ surface. Our simulations show that they tend to be adsorbed on Ba site on TiO_2 terminated surface while adsorbed on Ti sites on BaO terminated surface. A more detailed investigation of the adsorption mechanism in the $BaTiO_3$–NaOH–KOH interface will be presented in a separate study.

Furthermore, when excess water is present in the system, the reactivity of the surface changes due to a strongly adsorbed water layer on the $BaTiO_3$ surface (Supplementary Data, Figure S 2). This layer creates a barrier for interactions between alkali ions and the $BaTiO_3$ surface, preventing sufficient congruent dissolution in the system to drive densification.

We should note that the presence of limited amounts of water in the system does not create a dramatic effect on the reactivity of the surface; in contrast, a small amount of water is produced by the oxolation reactions between NaOH and KOH molten salts and is a part of chemistry in this interface. When flux systems are used, finding the right balance between their chemical reactivity to sufficiently dissolve oxide surfaces and their viscosity to facilitate the mass transport of dissolved species is important to densify ceramics.

- **Magnetite (Fe_3O_4)** is an important material for both applied technologies and basic science. Fe_3O_4 with a spinel structure is mainly investigated for applications such as biomedicine [63], catalysis [64], environmental remediation [64,65] and data storage [66] among others; whether as nanoparticles, bulk materials or both. The CSP of Fe_3O_4 was investigated using two types of transient liquids: Ethylenediaminetetraacetic acid (EDTA) and deep eutectic solvents.

Ethylenediaminetetraacetic acid (EDTA) is one of the most commonly used chelating reagent and organic acid to dissolve Fe_3O_4 [67,68], as it adsorbs on Fe(II) and Fe(III) to form Fe-EDTA complexes. These types of chelates can drive the chemical effects in cold sintering when a ligand exchange is possible with the grain surface, with a low activation barrier. The CSP of Fe_3O_4 with EDTA leads to an approximatively 80% dense magnetite.

One of the strategies to increase of the relative density of this material by CSP would be the use of chelating reagents that lead to coordination complexes with stability constants lower than EDTA's. In Table 1, Pyrazinecarboxylic acid, Methionine –N, *N*- diacetic acid and Methylenephosphonic acid would probably be better chelating reagents than EDTA or 2, 3- butylenedinitrilotetraacetic acid to aid CSP, as their corresponding coordination complexes have smaller stability constants and therefore low activation barriers for ligand exchange with oxide surfaces. Investigations to verify this assumption will have to be conducted.

Other types of high polarity liquids, deep eutectic solvents (DESs),

Table 1
Stability constants (log K) of coordination complexes with Fe^{2+} and Fe^{3+} metal ions (M) and different ligands (L), obtained from different equilibrium reactions at constant ionic strength μ (μ = 0.1) and temperature T (T = 25 °C). For log K values with *, μ = 1.0. As an example, $ML_2/M.L^2$ for Fe^{2+} and Pyrazinecarboxylic acid ($C_5H_4O_2N_2$) would represent $Fe^{2+} + 2C_5H_4O_2N_2 - Fe(C_5H_4O_2N_2)_2$ [69].

Chelating reagent (L)	Equilibrium reaction	Metal ion (M) and stability constants (log K)	
		Fe^{2+}	Fe^{3+}
Ethylenediaminetetraacetic acid (EDTA)	ML/M.L	14.30	25.10
2, 3- butylenedinitrilotetraacetic acid ($C_{12}H_{20}O_8N_2$)	ML/M.L	17.08	28.05
Pyrazinecarboxylic acid ($C_5H_4O_2N_2$)	ML/M.L	4.10*	7.50*
	$ML_2/M.L^2$	7.71*	10.40*
Methionine –N, *N*- diacetic acid ($C_9H_{15}O_6N_5$)	MHL/M.HL	4.68	10.98
	MHL/ML.H	9.02	3.18
Methylenephosphonic acid (Iminobis) ($C_2H_9O_6NP_2$)	MHL/M.LH	6.65	3.90

Table 2
Stability constants (log K) of coordination complexes with Ni^{2+}, Cu^{2+} and Zn^{2+} metal ions (M) and different ligands (L), for different equilibrium reactions at constant ionic strength μ (μ = 0.1) and temperature T (T = 25 °C). As an example, $ML_2/M.L^2$ for Ni^{2+} and Acetylacetone ($C_5H_8O_2$) would represent $Ni^{2+}+ 2C_5H_8O_2-$ $Ni(C_5H_7O_2)_2$ [69].

Ligand (L) of the coordination complex	Equilibrium reaction	Metal ion (M) and stability constants (log K)		
		Ni^{2+}	Cu^{2+}	Zn^{2+}
Acetylacetone ($C_5H_8O_2$)	ML/M.L	5.70	8.00	4.69
	$ML_2/M.L^2$	10.20	14.70	8.10
L-2-Amino-3-(4-hydroxyphenyl) propanoic acid (tyrosine) ($C_9H_{11}O_3N$)	MHL/M.HL	5.07	7.85	4.22
L-2, 5-Diaminopentanoic acid (ornithine) ($C_5H_{12}O_2N_2$)	MHL/M.HL	4.60	7.36	3.75
Pyrrole-2-carboxylic acid ($C_5H_{12}O_2N_2$)	ML/M.L	1.40	1.79	–
Triethylenetetramine	ML/M.L	13.80	20.05	12.00
Ethylenediaminetetraacetic acid (EDTA)	ML/M.L	18.40	18.80	16.50

have also been investigated for cold sintering. Deep eutectic solvents are a class of ionic liquids obtained by depressing the glass transition of a salt by complexing it with hydrogen bond donor molecules at the eutectic molar ratio [50–52,70]. Metal oxides exhibit high solubility in deep eutectic solvents composed of a 1:1 ratio between choline chloride (salt) and malonic acid (hydrogen bond donor). This may originate from the protons acting as good oxygen acceptors to enable the formation of chlorometalate species [52]. When 10 wt% of this eutectic solvent is used to cold sinter Fe_3O_4 under 320 MPa for 30 min, a microstructure with no obvious pores, nanograins embedded in a matrix is observed when a sintering temperature of 100 °C is applied (Fig. 6a). When the sintering temperature is increased to 180 °C, a few pores start to appear in the Fe_3O_4 microstructure (Fig. 6b). When two step sintering is applied under 320 MPa, with a first dwell at 100 °C for 30 min and a second one slightly above the decomposition temperature of the eutectic liquid (Supplementary Data, Figure S 4) at 300 °C for 60 min, a porous Fe_3O_4 ceramic with a vermicular-type of microstructure is obtained (Fig. 6c). By comparing Fe_3O_4 ceramics in Fig. 6a and c, differentiated by this additional heat treatment at 300 °C, we can assume that this last heating step led to the decomposition of residual eutectic liquid that persist in the Fe_3O_4 ceramic sintered at 100 °C (matrix in Fig. 6a). The use of eutectic solvents is promising but requires further investigation to reach high relative densities with a minimum of residual solvent.

- **Ferrite spinels:** Funahashi et al. [54] recently demonstrated that chelates and a solvent can be directly mixed with a ceramic powder to aid in densification by CSP. High relative density spinels such as Ni–Cu–Zn ferrites, Ni–Mn thermistors were obtained under 1 GPa at 300 °C using 10 wt % acetylacetonate and 10 wt % of water. The authors highlighted an approximately 20% relative density difference between ceramics obtained with this chelate solution and pure water as transient liquid. They also pointed out that the use of an excess amount of acetylacetone may prevent the important transient reactions and lead to low density materials. Resources in the literature on this approach are currently limited to one patent application [71] and one publication [54]. The densification of a broader group of ceramics is currently under investigation using this densification approach by "direct" precipitation of chemical species. As previously discussed, coordination complexes with low stability constants may be more efficient to aid CSP. Considering this assumption, chelates in Table 2 such as tyrosinates, ornithinates and Pyrrole-2-carboxylic acid-based complexes would be more efficient than acetylacetonates to drive CSP as they have low stability constants. However, the use of Triethylenetetramine or EDTA-based chelates with higher stability constants would not be beneficial to CSP.

3.2.1.2. Influence of the starting powder: Example of templated grain growth using cold sintering. The nature of the starting powder can affect the free-energy landscape of a system during sintering. Here, we show an example of templated grain growth using cold sintering. The starting powder used is a composed of a $BaTiO_3$ matrix powder and template particles (Figure S 3) (5 wt %), mixed with 10 wt% of NaOH–KOH as a transient flux prior to applying different sintering conditions (see Supplementary Data, Procedure SP2 for detailed sintering protocols). The templated grain growth observed after CSP followed by annealing and also conventional sintering of the mixture is discussed.

For the as-cold sintered sample (Fig. 7a), a ceramic with large single crystal grains (from the template) and a dense fine-grained polycrystalline matrix is obtained. No obvious lateral growth of the template occurs, but there is a clear interface between the matrix and the template. During CSP, in spite of the presence of highly reactive molten hydroxides, the driving potential for mass transport is decreased from matrix grains to templates as the surface energy of their face perpendicular to the c-axis <001> is low [72]. Thicknesses of templates and grain sizes in the matrix increase after annealing the as-cold sintered sample at 740 °C for 5 h (Fig. 7b). On the one hand, grains in the matrix grow *via* classic solid-state diffusion mechanisms probably enhanced by hydroxide traces at grain boundaries; on the other hand, epitaxial nucleation of matrix grains on $BaTiO_3$ templates help grow the latter. Knowing that the as-cold sintered sample has a relative density of ~95% and therefore low surface area, the further decrease in the Gibbs free-energy (Fig. 7e) is driven by the variation of energy at $BaTiO_3/BaTiO_3$ interfaces. This shows that the as-cold sintered sample in this specific material system is

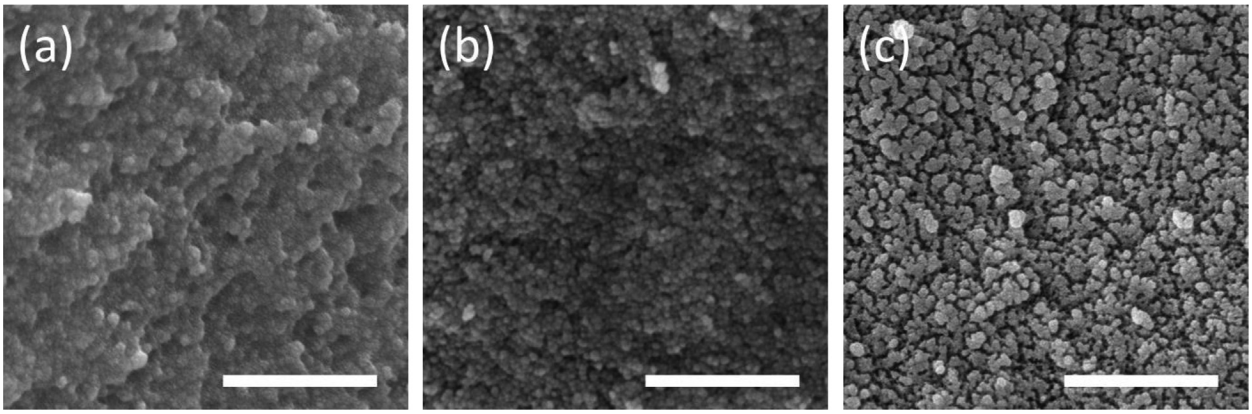

Fig. 6. SEM images of Fe_3O_4 cold sintered under 320 MPa with a deep eutectic solvent (Choline chloride: malonic acid, 1:1 ratio) and (a) 100 °C, 30 min, (b) 180 °C, 30 min and (c) 100 °C, 30 min - 300 °C, 60 min. Scale bar: 500 nm.

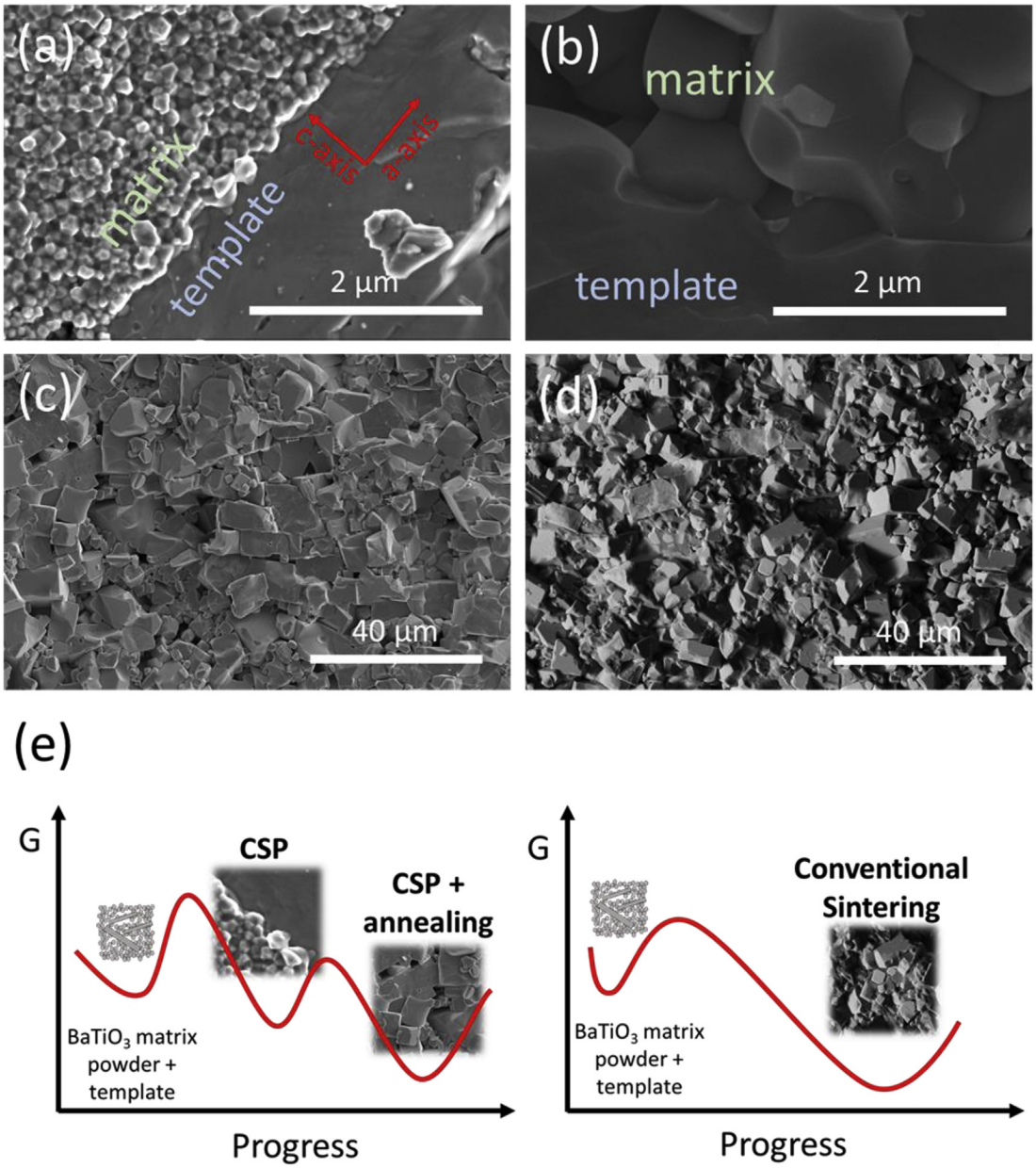

Fig. 7. SEM images of $BaTiO_3$ obtained by (a) CSP at 300 °C, 340 MPa and 5 h; CSP (300 °C, 340 MPa, 5 h) followed by annealing under air at (b) 740 °C and (c) 800 °C for 5 h. (d) SEM images of $BaTiO_3$ obtained by conventional sintering at 800 °C for 5 h under air. (e) Free energy landscape of the system composed of a mixture of $BaTiO_3$ matrix powder and template powder during CSP followed by annealing and conventional sintering.

metastable, owing to its high energy grain boundaries. Further templated grain growth takes place when the as-cold sintered sample is annealed at 800 °C for 5 h, with mechanisms similar to those previously discussed. The final ceramic does not contain a significant number of small grains.

For the sample conventionally sintered at 800 °C for 5 h, a dense ceramic is obtained with smaller and more randomly orientated grains (Fig. 7d), compared to the cold sintered specimen annealed at 800 °C (Fig. 7c). NaOH–KOH eutectic additives (10 wt%) in the starting $BaTiO_3$ mixture remains liquid from 170 °C up to the used sintering temperature. The presence of this liquid phase increases the kinetics of grain boundary migration and the mechanism of crystal growth is based on dissolution of the polycrystalline matrix grains and deposition in the lowest energy surface in the system [73]. In conventional sintering, the free energy barrier to sintering is surmounted thanks to high temperatures, which also steadily lead the system to a minimum energy level (Fig. 7e).

3.2.2. *Pathway A → B*

In the pathway for densification A → B, the final material has a different chemical composition or a crystallographic phase than the initial powder or by allotropic change or by the formation of a new compound.

3.2.2.1. Allotropic change. The cold sintering offers the possibility to obtain dense ceramics through phase transition. As an example, a dense α-quartz ceramics was obtained by cold sintering amorphous SiO_2 powders with a 5 M NaOH solution, under 350 MPa and 270 °C [74]. The sintering behavior of the system was composed of multiple steps (Fig. 8) [74]: (a) the densification of an amorphous matrix, following a pressure solution mechanism (Figs. 8, 12 min) (b) Na ions present in the material depolymerization of the silica network to form a very compact and metastable amorphous silica matrix (invert glass) that may be composed

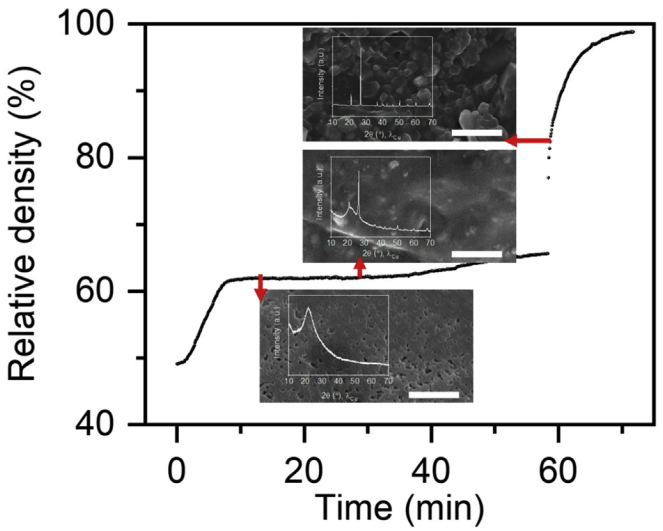

Fig. 8. Timely evolution of the relative density, microstructure and phase during the CSP of amorphous SiO_2 with 5 M NaOH. SEM images and XRD patterns of quenched samples are shown for sintering times of 12, 28 and 59 min. Scale bar: 1 μm.

of SiO_4 tetrahedra and Si_2O_7 dimers. α-quartz nuclei and nanocrystals are embedded in the invert glass (Fig. 8, 28min) the depolymerization of the Si–O–Si network in the matrix to form and the nucleation of α-quartz, (c) and finally the abrupt growth of α-quartz crystals (Fig. 8, 59min) most likely by particle attachment, a non-classical pathway for crystal growth described by de Yoreo et al. [75].

Similar behaviors may be expected for a variety of amorphous materials that can undergo an important network depolymerization.

The phase transition of $LiMoO_4$ from phenacite to spinel was shown by Floyd et al. [30] The spinel, a high pressure phase, began to form less than 10 min after the CSP of phenacite and 6 wt% of water at 120 °C and 700 MPa. This highlights the possibility of pressure-induced allotropic change under the CSP.

3.2.2.2. Formation of a new compound. Dense ceramics can be obtained by CSP using a "precursor" approach, where the starting powder loses inorganic functional groups and/or chemisorbed water to form the most thermodynamically stable oxide under the applied conditions. This approach has also been used in spark plasma sintering by Elissalde et al. [76] to sinter nanocrystalline ZrO_2 in a single step at 350 °C. The densification of Fe_2O_3 with this approach was investigated by CSP. An iron oxyhydroxide, goethite (α-FeOOH), was used as precursor. A salt, Iron trichloride - $FeCl_3$ (20 wt%), was used for densification of the ceramic under 530 MPa, for 60 min and 180 min. The sintering temperature of 310 °C was carefully chosen between the melting (306 °C) and the decomposition temperature (316 °C) of $FeCl_3$. A relative density of 97% (of the real density 5.14 g cm^{-3}, measured by He pycnometry) was obtained after 60 min of dwell time. The microstructure shows the presence of both micron-sized and nanosized grains (Fig. 9 a). At higher magnification (inset Fig. 9 a) one can distinguish ongoing Ostwald ripening mechanism [77], where small grains are consumed by bigger ones. EDS mapping (Fig. 9c-e) shows that the ceramic contains Fe and O elements only. This is confirmed by the EDS spectrum (Fig. 9 f), which also highlights that there are trace residue levels of chlorine (Cl) from the $FeCl_3$ salt. During the sintering, an important degassing phenomenon is observed from 270 °C. At this temperature, α-FeOOH decomposes by dehydroxylation as shown by thermogravimetric analysis available in the literature [78,79]. The decomposition at this stage may lead to the formation of α- Fe_2O_3, a small amount of Fe_3O_4 and H_2O. Then, H_2O molecules released by dehydroxylation participate in the hydrolysis of $FeCl_3$ into form α- Fe_2O_3 [80,81], due to the presence of α- Fe_2O_3 seeds from the first reaction. Indeed, Atkinson et al. [81] have shown that without α- Fe_2O_3 seeds, hydrolysis of $FeCl_3$ leads to the formation of β - FeOOH particles. These observations are consistent with XRD analyses (Fig. 9 g), showing that besides the main phase α- Fe_2O_3, small amounts of the precursor FeOOH and Fe_3O_4 impurities are detected.

The presence of the precursor after a 60 min dwell time confirms ongoing reactions and the necessity of a longer reaction time. With an 180 min dwell time, a phase pure α- Fe_2O_3 ceramic (Fig. 9g) with a microstructure consisting of few nanograins (Fig. 9b) is obtained. Larger grains are obtained, probably *via* the previously observed Ostwald ripening mechanism. The pure α- Fe_2O_3 ceramic has a relative density of 89%. These newly-generated pores may come from the volume change ($\Delta V/V_0 \approx$ -18.9%) occurring during the α- FeOOH (4.25 g cm^{-3}) → α-Fe_2O_3 (5.24 g cm^{-3}) transformation of the impurity.

3.2.3. Pathway A + B → C

The pathway A + B → C or reactive cold sintering, takes place when a mixture of precursors that can react together in cold sintering conditions to yield a new material or a doped compound. This approach is inspired by different low temperature reactive (a) synthesis techniques using small amounts of solvents such as the water assisted solid-state reaction [82–86], salt melt synthesis with their high reactivity [53] and (b) densification techniques such as the reactive hydrothermal densification [18].

3.2.3.1. Doping. The doping of ceramics can occur during cold sintering, when optimum conditions are identified (T, P, t, liquid/flux). The dopant precursor needs to be carefully chosen as it should dissociate under the chosen processing conditions and react with the oxide before the precipitation step of pressure solution creep. There are not extensive investigations on this approach in the literature, however the doping phenomena was experimentally observed for CeO_2 and $BaTiO_3$. Here, we briefly discuss about the doping of $BaTiO_3$ using CSP.

Chemical doping of $BaTiO_3$ takes place when the selected transient flux participates in the reaction before or during the precipitation step of pressure solution creep. If we compare $BaTiO_3$ ceramics cold sintered under similar processing conditions and different fluxes: $Ba(OH)_2{\cdot}8H_2O$ and $Sr(OH)_2{\cdot}8H_2O$, the relative density is 95% and 92% of the theoretical density of pure $BaTiO_3$ (6.03 g cm^{-1}), respectively. Dense and homogeneous microstructures, with multifaceted nanograins (Fig. 10 a and b) and high phase purity (Fig. 10 c) are obtained in both cases. The formation of a $Ba_{1-x}Sr_xTiO_3$ solid solution is confirmed by a decrease of the Curie temperature (Fig. 10 c) and peak shifts in XRD patterns towards higher angles (inset Fig. 10 c), as a result of a lattice contraction as Ba^{2+} ions ($r_{Ba^{2+}}$ = 149 p.m.) are partially substituted by smaller cations (Sr^{2+} ions, $r_{Sr^{2+}}$ = 132 p.m.). Fig. 10 d shows that the sintering temperature is also a parameter to consider for the tuning and control of the substitution level in the solid solution as it influences the reactivity of fluxes. This promising approach needs to be thoroughly investigated as it may allow to tune/enhance functional properties of ceramics densified in a single step at record low temperatures.

3.2.3.2. Formation of a new compound. The reactive densification of ceramics is commonly used through solid-state diffusion approaches [87, 88] or under hydrothermal conditions from a porous preform as described by Riman et al. with the reactive hydrothermal liquid phase densification (rLHPD) [18]. In cold sintering, this approach can be used with a simple mixture of precursor powders and a solvent. Although phase pure ceramics have not yet been achieved with this approach in a single step, it is a promising route for the fabrication of dense and multicationic compounds. Here, an example of the reactive sintering using CSP to obtain dense zinc ferrite ($ZnFe_2O_4$) is demonstrated. A 2:1 M ratio of goethite (α-FeOOH) and zinc hydroxide ($Zn(OH)_2$) were mixed prior to

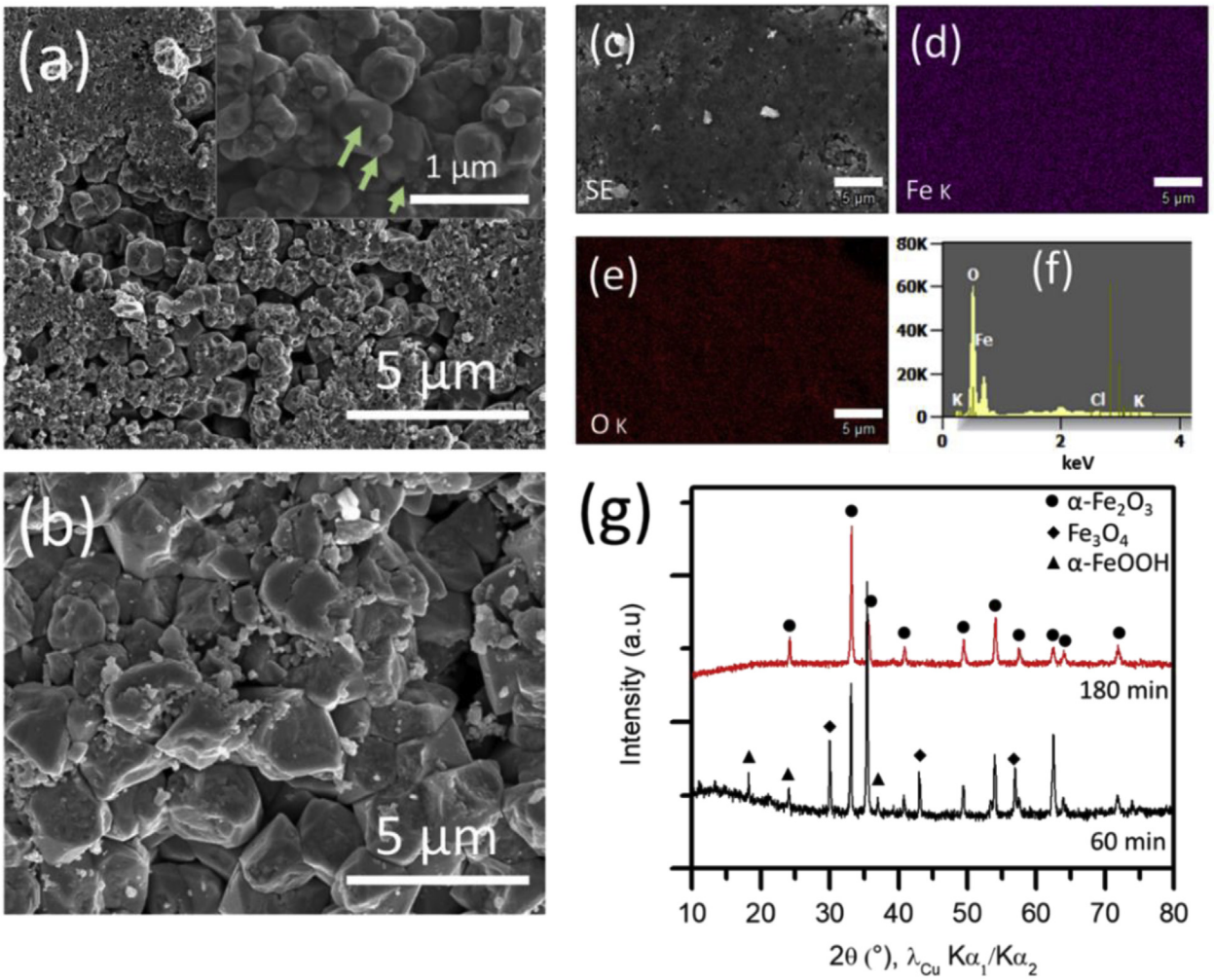

Fig. 9. SEM image of the ceramic resulting from the CSP of α-FeOOH with 20 wt% of molten $FeCl_3$, under 530 MPa, at 310 °C and for (a) 60 min at low and high magnification (inset); the green arrows highlight features of an ongoing Ostwald ripening mechanism; (b) 180 min. (c–f) EDS analysis of the α-FeOOH ceramic cold sintered for 60 min, with simultaneous acquisition of: (c) Secondary electron (SE) image and elemental maps of (d) iron (Fe), (e) oxygen (O) and (f) EDS spectrum. (g) X-Ray diffraction (XRD) patterns of α-FeOOH cold sintered for 60 and 180 min. (For interpretation of the references to color in this figure legend, the reader is referred to the Web version of this article.)

sintering using 10 vol% of a NaOH–KOH eutectic flux. An almost fully dense ceramic, (~97% of relative density) with multifaceted sub-micrometer grains (Fig. 11a) was obtained at 395 °C and 530 MPa. The obtained ceramic is in fact a composite with $ZnFe_2O_4$ as main phase (Phase volume fraction of 41.0%, approximated with the software Jade - Supplementary Data, Figure S 5) and ZnO (28%), Fe_2O_3 (20%), Fe_3O_4 (12%) as secondary phases (Fig. 11e).

Kleshchev et al. synthesized pure $ZnFe_2O_4$ particles by hydrothermal method with similar precursors (α-FeOOH and $Zn(OH)_2$) and molar ratio (2:1). The proposed mechanism for $ZnFe_2O_4$ formation is dissolution-precipitation, during which the new phase is obtained by heterogeneous nucleation. The nucleation is preceded by the chemical transformation of α-FeOOH and $Zn(OH)_2$ to their corresponding oxides [89]. The chemical transformation of hydroxides in molten oxosalts is not widely discussed in the literature. It would be premature to propose a precursor chemical transformation pathway which drives the described process. However, considering the homogeneous microstructure (Fig. 11a), homogeneous elemental distribution of Fe (Fig. 11d) and less homogeneous distribution of Zn (Fig. 11c) obtained after CSP, it appears that $ZnFe_2O_4$ forms through nucleation and epitaxial growth on ZnO and iron oxide surfaces.

4. Conclusions and perspectives

4.1. Conclusions

In this review, we highlight different pathways towards low temperature densification of materials, based on experimentally-evidenced CSP results. (a) In the pathway A → A, the initial powder has the same chemical composition and crystallographic phase as the densified material. (b) In the pathway A → B, the final material has a different chemical composition or crystallographic phase than the initial powder. Changes in chemical compositions can be obtained by dehydration/decomposition reactions *via* a "precursor" approach. Allotropic changes during CSP can be thermally- or pressure-induced. (c) The pathway A + B → C is a reactive route, where a mixture of compounds can lead to a chemical doping or to a new compound after CSP. For all the pathways, it was shown that dissolution, speciation, species concentration and stability were critical factors to efficiently drive the sintering process. In the reactive pathway, the reactivity between species is also important, but not fully optimized for most of the material systems to obtain pure phases. All these aspects are influenced by solvent selection, which is the critical step of CSP. This includes the co-firing of composites, where the

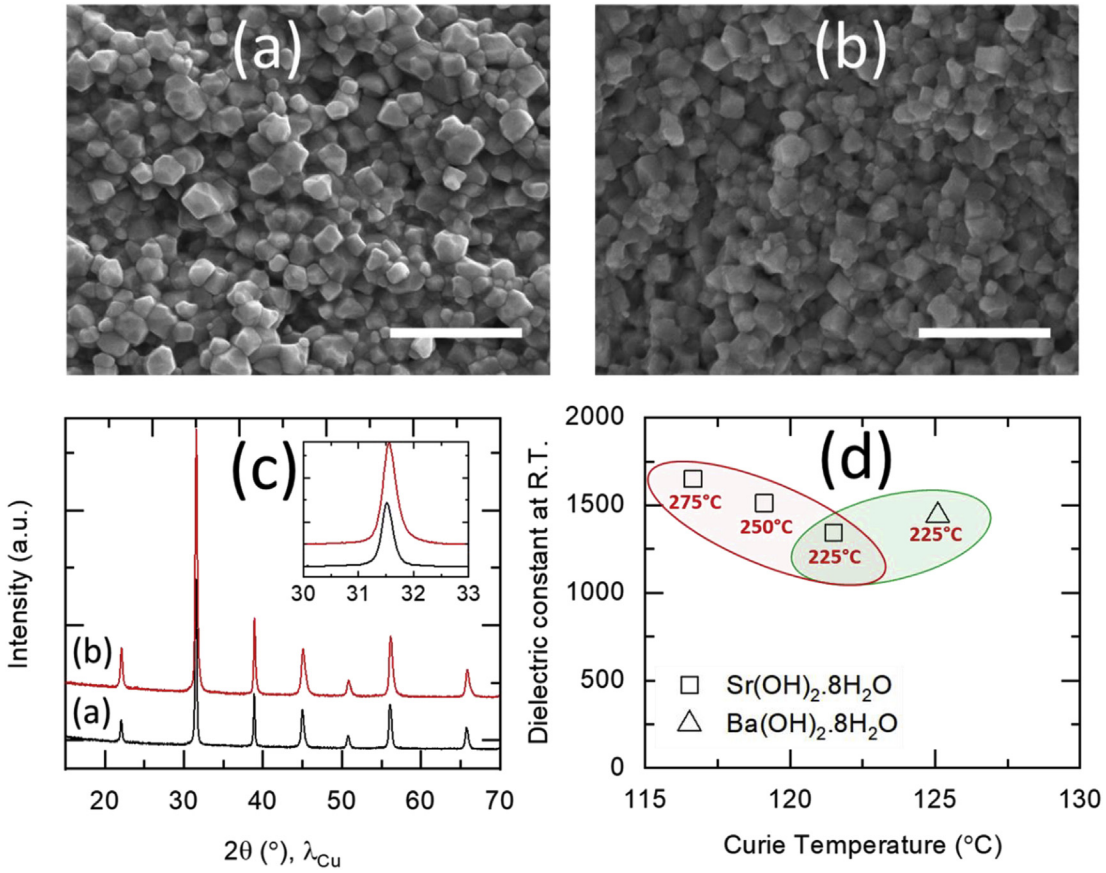

Fig. 10. (a-b)SEM images and XRD patterns (c) of $BaTiO_3$ cold sintered at 225 °C, 350 MPa, 60 min using (a) $Ba(OH)_2{\cdot}8H_2O$ and (b) $Sr(OH)_2{\cdot}8H_2O$ fluxes. Scale bar: 500 nm. Curie temperature and room temperature (R.T.) dielectric constant of several $Ba_{1-x}Sr_xTiO_3$ ceramics obtained with different fluxes or sintering temperatures (shown under the points).

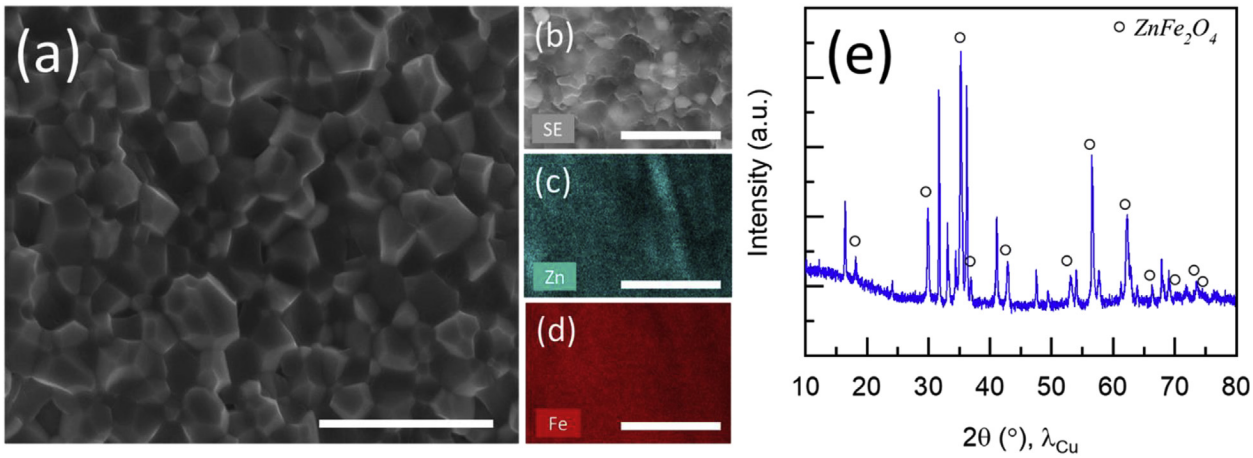

Fig. 11. (a) SEM image and (e) XRD pattern of the ceramic resulting from the CSP of goethite (α-FeOOH) and zinc hydroxide ($Zn(OH)_2$) in a 2:1 M ratio, with a NaOH–KOH eutectic flux at 395 °C, 530 MPa and 60 min. Peaks of $ZnFe_2O_4$, the main phase, are highlighted (b–d) EDS analysis of the cold sintered ceramic with (b) Secondary electron (SE) image and elemental maps of (c) zinc (Zn), (d) iron (Fe). Scale bars: 2 μm.

selected solvent also needs to be compatible with all of the constituent compounds to densify. Solvents are not limited to water or aqueous solvents: other solvents include polar/semi-polar non-aqueous liquids with low evaporation temperatures, ionic eutectic salt melts, as well as solvent-chelating agent mixtures. In some cases, hydrated solids that decompose during the process can also drive densification, such as in the cases of hydrated Zn-acetate and Ba-hydroxide hydrate. On a more fundamental aspect, theoretical models adapted for cold sintering based on the coupling of non-equilibrium thermodynamics and thermodynamic laws of non-hydrostatically stressed solids defined by the Gibbs-Kamb theory will need to be carefully developed.

4.2. Perspectives

A deeper understanding of underlying mechanisms requires the development of new tools and equipment for *in situ* investigations of

solid-fluid interface-coupled reactions for dissolution and precipitation under the variables of temperature and pressure. The importance of speciation, stability of species and energies to overcome for an efficient ligand exchange on the oxide surfaces are evidenced by ReaxFF molecular dynamics method. Machine learning approaches may be very helpful to facilitate solvent selection for a given material, by considering detailed physical and chemical characteristics of both candidate solvents and the oxide surface to cold sinter. For example, a database involving correlations between decomposition temperature of the used solvent, stability of species at the interface, dissolvability of the oxide surface and sinterability of materials of interest would be generated to predict appropriate solvent-material pairs for future studies and understand trends using supervised machine learning techniques.

Declaration of interests

The authors declare that they have no known competing financial interests or personal relationships that could have appeared to influence the work reported in this paper.

Acknowledgment

This work was supported by Murata Manufacturing Co., Ltd (funding ITO-009, A.N., C.A.R.), the U.S. National Science Foundation (DMR-1728634: C.A.R., S.H.B; DMR-1842922 and MRI-1626251: A.C.T.vD, M.Y.S.; IIP-1841453 and 1841466 as part of the Center for Dielectric and Piezoelectric: K.T.), the AFOSR grant (grant no. FA9550-16-1-0429, C.A.R., A.N., Z.A.G., S.D.) and Kyocera fellow (T.S.).

Appendix A. Supplementary data

Supplementary data to this article can be found online at https://doi.org/10.1016/j.oceram.2020.100019.

References

[1] D.M. Roy, G.R. Gouda, A. Bobrowsky, Very high strength cement pastes prepared by hot pressing and other high pressure techniques, Cement Concr. Res. 2 (1972) 349–366.
[2] D.M. Roy, G. Gouda, High strength generation in cement pastes, Cement Concr. Res. 3 (1973) 807–820.
[3] H. Toraya, M. Yoshimura, S. Sōmiya, Hydrothermal reaction - sintering of monoclinic HfO2, J. Am. Ceram. Soc. 65 (1982) c159–c160, https://doi.org/10.1111/j.1151-2916.1982.tb10527.x.
[4] S.-I. Hirano, S. Sōmiya, Hydrothermal reaction sintering of pure Cr2O3, J. Am. Ceram. Soc. 59 (1976) 534, https://doi.org/10.1111/j.1151-2916.1976.tb09432.x.
[5] N. Yamasaki, K. Yanagisawa, M. Nishioka, S. Kanahara, A hydrothermal hot-pressing method: apparatus and application, J. Mater. Sci. Lett. 5 (1986) 355–356, https://doi.org/10.1007/BF01748104.
[6] Y. Xie, S. Yin, H. Yamane, T. Hashimoto, T. Sato, Low temperature sintering and color of a new compound Sn1.24Ti1.94O3.66(OH)1.50F1.42, Solid State Sci. 11 (2009) 1703–1708, https://doi.org/10.1016/j.solidstatesciences.2009.05.025.
[7] N. Yamasaki, T. Weiping, K. Jiajun, Low-temperature sintering of calcium carbonate by a hydrothermal hot-pressing technique, J. Mater. Sci. Lett. 11 (1992) 934–936.
[8] N. Yamasaki, T. Kai, M. Nishioka, K. Yanagisawa, K. Ioku, Porous hydroxyapatite ceramics prepared by hydrothermal hot pressing, J. Mater. Sci. Lett. 9 (1990) 1150.
[9] K. Yanagisawa, M. Nishioka, K. Ioku, N. Yamasaki, Neck formation of spherical silica particles by hydrothermal hot pressing, J. Mater. Sci. Lett. 9 (1990) 7–8, https://doi.org/10.1007/BF00724415.
[10] S. Katsuyama, Y. Takiguchi, M. Ito, Synthesis of Ca3Co4O9 ceramics by citric acid complex and hydrothermal hot-pressing processes and investigation of its thermoelectric properties, Mater. Trans. 48 (2007) 2073–2078, https://doi.org/10.2320/matertrans.E-MRA2007805.
[11] G. Goglio, A. Largeteau, A. Ndayishimiye, M. Prakasam, Procédé et dispositif de densification des matériaux ou de consolidation d'un assemblage de matériaux par frittage hydrothermal ou solvothermal, 2018.
[12] G. Goglio, A. Ndayishimiye, A. Largeteau, C. Elissalde, View point on hydrothermal sintering: main features, today's recent advances and tomorrow's promises, Scripta Mater. 158 (2019) 146–152, https://doi.org/10.1016/j.scriptamat.2018.08.038.
[13] A. Ndayishimiye, A. Largeteau, S. Mornet, M. Duttine, M.-A. Dourges, D. Denux, M. Verdier, M. Gouné, T. Hérisson de Beauvoir, C. Elissalde, G. Goglio, Hydrothermal sintering for densification of silica. Evidence for the role of water, J. Eur. Ceram. Soc. 38 (2018) 1860–1870, https://doi.org/10.1016/j.jeurceramsoc.2017.10.011.
[14] A. Ndayishimiye, S. Buffière, M.A. Dourges, A. Largeteau, M. Prakasam, S. Mornet, O. Kaman, J. Zdeněk, J. Hejtmánek, G. Goglio, Design of 0–3 type nanocomposites using hydrothermal sintering, Scripta Mater. 148 (2018) 15–19, https://doi.org/10.1016/j.scriptamat.2018.01.013.
[15] O. Kaman, Z. Jirak, J. Hejtmánek, A. Ndayishimiye, M. Prakasam, G. Goglio, Tunneling magnetoresistance of hydrothermally sintered La1-xSrxMnO3-silica nanocomposites.pdf, J. Magn. Magn Mater. 479 (2019) 135–143.
[16] M. Prakasam, A. Morvan, C. Azina, L. Constantin, G. Goglio, A. Largeteau, S. Bordère, J.-M. Heintz, Y. Lu, J.-F. Silvain, Ultra-low temperature fabrication of copper carbon fibre composites by hydrothermal sintering for heat sinks with enhanced thermal efficiency, Compos. Part A Appl. Sci. Manuf 133 (2020) 105858, https://doi.org/10.1016/j.compositesa.2020.105858.
[17] R.E. Riman, V. Atakan, Method of hydrothermal liquid phase sintering of ceramic materials and products devired therefrom, US Patent 8,313,802 (2012) and 8,709,960(2014), n.d.
[18] C. Vakifahmetoglu, J.F. Anger, V. Atakan, S. Quinn, S. Gupta, Q. Li, L. Tang, R.E. Riman, Reactive hydrothermal liquid-phase densification (rHLPD) of ceramics. A study of the BaTiO3[TiO2] composite system, J. Am. Ceram. Soc. 99 (2016) 3893–3901, https://doi.org/10.1111/jace.14468.
[19] Q. Li, S. Gupta, L. Tang, S. Quinn, V. Atakan, R.E. Riman, A novel strategy for carbon capture and sequestration by rHLPD processing, Front. Energy Res. 3 (2016) 1–11, https://doi.org/10.3389/fenrg.2015.00053.
[20] C. Vakifahmetoglu, L. Karacasulu, Cold sintering of ceramics and glasses: a review, Curr. Opin. Solid State Mater. Sci. (2020) 100807.
[21] S. Grasso, M. Biesuz, L. Zoli, G. Taveri, A.I. Duff, D. Ke, A. Jiang, M.J. Reece, A review of cold sintering processes, Adv. Appl. Ceram (2020) 1–29.
[22] T. Ibn-mohammed, C.A. Randall, K.B. Mustapha, J. Guo, J. Walker, S. Berbano, Decarbonising ceramic manufacturing : a techno-economic analysis of energy e ffi cient sintering technologies in the functional materials sector, J. Eur. Ceram. Soc. 39 (2019) 5213–5235, https://doi.org/10.1016/j.jeurceramsoc.2019.08.011.
[23] H. Guo, A. Baker, J. Guo, C.A. Randall, Protocol for ultralow-temperature ceramic sintering: an integration of nanotechnology and the cold sintering process, ACS Nano 10 (2016) 10606–10614, https://doi.org/10.1021/acsnano.6b03800.
[24] J. Guo, H. Guo, A.L. Baker, M.T. Lanagan, E.R. Kupp, G.L. Messing, C.A. Randall, Cold sintering: a paradigm shift for processing and integration of ceramics, Angew. Chemie - Int 55 (2016) 11457–11461, https://doi.org/10.1002/anie.201605443.
[25] J.-P. Gratier, D.K. Dysthe, F. Renard, The role of pressure solution creep in the ductility of the Earth's upper crust, Adv. Geophys. 54 (2013) 47–179.
[26] J. Guo, R. Floyd, S. Lowum, J. Maria, T. Herisson De Beauvoir, J.-H. Seo, C.A. Randall, Cold Sintering ;: progress, challenges, and future opportunities, Annu. Rev. Mater. Res. 49 (2019) 275–295.
[27] A. Baker, H. Guo, J. Guo, C. Randall, Utilizing the cold sintering process for flexible-printable electroceramic device fabrication, J. Am. Ceram. Soc. 3 (2016) 1–3, https://doi.org/10.1111/jace.14467.
[28] H. Kähäri, M. Teirikangas, J. Juuti, H. Jantunen, Dielectric properties of lithium molybdate ceramic fabricated at room temperature, J. Am. Ceram. Soc. 97 (2014) 3378–3379, https://doi.org/10.1111/jace.13277.
[29] T. Hérisson de Beauvoir, S. Dursun, L. Gao, C. Randall, New opportunities in metallization integration in Co fi red electroceramic multilayers by the cold sintering process´, ACS Appl. Electron. Mater 1 (2019) 1198–1207, https://doi.org/10.1021/acsaelm.9b00184.
[30] R. Floyd, S. Lowum, J.-P. Maria, Instrumentation for automated and quantitative low temperature compaction and sintering, Rev. Sci. Instrum. 90 (2019) 55104, https://doi.org/10.1063/1.5094040, 1–8.
[31] C.L. Martin, D. Bouvard, S. Shima, Study of particle rearrangement during powder compaction by the Discrete Element Method, J. Mech. Phys. Solid. 51 (2003) 667–693, https://doi.org/10.1016/S0022-5096(02)00101-1, doi.
[32] J.L. Urai, C.J. Spiers, H.J. Zwart, G.S. Lister, Weakening of rock salt, Nature 324 (1986) 554–557.
[33] M.Y. Sengul, C.A. Randall, A.C.T. Van Duin, ReaxFF molecular dynamics study on the influence of temperature on adsorption, desorption, and decomposition at the acetic acid/water/ZnO (10 ¯10) interface enabling cold sintering, ACS Appl. Mater. Interfaces 10 (2018) 37717–37724, https://doi.org/10.1021/acsami.8b13630.
[34] M.Y. Sengul, C.A. Randall, A.C.T. Van Duin, ReaxFF molecular dynamics simulation of intermolecular structure formation in acetic acid-water mixtures at elevated temperatures and pressures, J. Chem. Phys. 148 (2018) 164506, https://doi.org/10.1063/1.5025932, 1–6.
[35] M.Y. Sengul, J. Guo, C.A. Randall, A.C.T. Van Duin, Water-mediated surface diffusion mechanism enabling the Cold Sintering Process: a combined computational and experimental study, Angew. Chem. Int. Ed. 58 (2019) 12420–12424, https://doi.org/10.1002/ange.201904738.
[36] J. Gonzalez-Julian, K. Neuhaus, M. Bernemann, J. Pereira da Silva, A. Laptev, M. Bram, O. Guillon, Unveiling the mechanisms of cold sintering of ZnO at 250°C by varying applied stress and characterizing grain boundaries by Kelvin Probe Force Microscopy, Acta Mater. 144 (2018) 116–128, https://doi.org/10.1016/j.actamat.2017.10.055.
[37] H.-Z. Shen, N. Guo, L. Zhao, P. Shen, Role of ion substitution and lattice water in the densification of cold-sintered hydroxyapatite, Scripta Mater. 177 (2020) 141–145, https://doi.org/10.1016/j.scriptamat.2019.10.024.
[38] H.C. Sorby, On the direct correlation of mechanical and chemical forces, The Bakerian Lecture (1863) 538–550.
[39] I. Shimizu, Kinetics of pressure solution creep in quartz: theoretical considerations, Tectonophysics 245 (1995) 121–134, https://doi.org/10.1016/0040-1951(94)00230-7.
[40] W.B. Kamb, The thermodynamic theory of nonhydrostatically stressed solids, J. Geophys. Res. 66 (1961).

[41] D.W. Durney, Solution - transfer, an important geological deformation mechanism, Nature 235 (1972) 315–317.
[42] E. Ruiz-Agudo, C.V. Putnis, Direct observations of mineral -fluid reactions using atomic force microscopy : the specific example of calcite, Mineral. Mag. 76 (2012) 227–253, https://doi.org/10.1180/minmag.2012.076.1.227.
[43] F. Renard, A. Røyne, C. V Putnis, Timescales of interface-coupled dissolution-precipitation reactions on carbonates, Geosci. Front 10 (2019) 17–27, https://doi.org/10.1016/j.gsf.2018.02.013.
[44] W.D. Kingery, J.M. Woulbroun, F.R. Charvat, Effects of applied pressure on densification during sintering in the presence of a liquid phase, J. Am. Ceram. Soc. 46 (1963) 391–395, https://doi.org/10.1111/j.1151-2916.1963.tb11758.x.
[45] H. Guo, A. Baker, J. Guo, C.A. Randall, D. Johnson, Cold sintering process: a novel technique for low-temperature ceramic processing of ferroelectrics,, J. Am. Ceram. Soc. 99 (2016) 3489–3507, https://doi.org/10.1111/jace.14554.
[46] K. Tsuji, A. Ndayishimiye, S. Lowum, R. Floyd, K. Wang, M. Wetherington, J. Maria, C.A. Randall, Single step densification of high permittivity BaTiO3 ceramics at 300°C, J. Eur. Ceram. Soc. 40 (2019) 1280–1284, https://doi.org/10.1016/j.jeurceramsoc.2019.12.022.
[47] Z. Grady, K. Tsuji, A. Ndayishimiye, J.-H. Seo, C.A. Randall, Densification of a solid-state NASICON sodium-ion electrolyte below 400°C by cold sintering with a fused hydroxide solvent, ACS Appl. Energy Mater. 3 (2020) 4356–4366, https://doi.org/10.1021/acsaem.0c00047.
[48] T.H. Zaengle, A. Ndayishimiye, K. Tsuji, Z. Fan, S.H. Bang, J. Perini, S.T. Misture, C.A. Randall, Single-step densification of nanocrystalline CeO2 by the cold sintering process, J. Am. Ceram. Soc. 103 (2020) 2979–2985, https://doi.org/10.1111/jace.17003.
[49] C.A. Randall, J. Guo, A.L. Baker, M.T. Lanagan, H. Guo, Cold Sinteing Ceramics and Composites, Patent Application US 2017/0088471 A1, 2017.
[50] R. Boston, P.Y. Foeller, D.C. Sinclair, I.M. Reaney, Synthesis of barium titanate using deep eutectic solvents, INORGA 56 (2017) 542–547, https://doi.org/10.1021/acs.inorgchem.6b02432.
[51] E.L. Smith, A.P. Abbott, K.S. Ryder, Deep eutectic solvents (DESs) and their applications, Chem. Rev. 114 (2014) 11060–11082, https://doi.org/10.1021/cr300162p.
[52] A.P. Abbott, G. Capper, D.L. Davies, K.J. Mckenzie, S.U. Obi, Solubility of metal oxides in deep eutectic solvents based on choline chloride, J. Chem. Eng. Data 51 (2006) 1280–1282, https://doi.org/10.1021/je060038c.
[53] X. Liu, N. Fechler, M. Antonietti, Salt melt synthesis of ceramics, semiconductors and carbon nanostructures, Chem. Soc. Rev. 42 (2013) 8237–8265, https://doi.org/10.1039/c3cs60159e.
[54] S. Funahashi, E. Kobayashi, M. Kimura, K. Shiratsuyu, C.A. Randall, Chelate complex assisted cold sintering for spinel ceramics, J. Ceram. Assoc. Japan 127 (2019) 899–904.
[55] A. Janotti, C.G. Van De Walle, Fundamentals of zinc oxide as a semiconductor, Rep. Prog. Phys. 72 (2009) 126501, https://doi.org/10.1088/0034-4885/72/12/126501, 1–29.
[56] X. Kang, R. Floyd, S. Lowum, M. Cabral, E. Dickey, J.-P. Maria, Mechanism studies of hydrothermal cold sintering of zinc oxide at near room temperature, J. Am. Ceram. Soc. 102 (2019) 4459–4469, https://doi.org/10.1111/jace.16340.
[57] S. Funahashi, J. Guo, H. Guo, K. Wang, A.L. Baker, K. Shiratsuyu, C.A. Randall, Demonstration of the cold sintering process study for the densification and grain growth of ZnO ceramics, J. Am. Ceram. Soc. 100 (2017) 546–553, https://doi.org/10.1111/jace.14617.
[58] M. Zhu, G. Pan, Quantum chemical studies of mononuclear zinc species of hydration and hydrolysis, J. Phys. Chem. 109 (2005) 7648–7652.
[59] S.H. Bang, A. Ndayishimiye, C.A. Randall, Anisothermal densification kinetics of cold sintering process below 150°C, J. Mater. Chem. C 8 (2020) 5668–5672, https://doi.org/10.1039/D0TC00395F.
[60] G.J. Janz, F.W. Dampier, G.R. Lakshminarayanan, P.K. Lorenz, R.P.T. Tomkins, Molten Salts: Volume 1, Electrical Conductance, Density, and Viscosity Data, NSRDS-NBS, Library of Congress Catalog Card N 68-60051, 1968.
[61] S. Zecchin, G. Schiavon, G.G. Bombi, Interdiffusion coefficient of water in molten hydroxides, Electroanal. Chem. Interfacial Electrochem 50 (1974) 261–267, https://doi.org/10.1016/S0022-0728(74)80157-9.
[62] D. Akbarian, D.E. Yilmaz, Y. Cao, P. Ganesh, I. Dabo, J. Munro, R. Van Ginhoven, A.C.T. van Duin, Understanding the influence of defects and surface chemistry on ferroelectric switching: a ReaxFF investigation of BaTiO3, Phys. Chem. Chem. Phys. 21 (2019) 18240–18249, https://doi.org/10.1039/c9cp02955a.
[63] S. Mornet, S. Vasseur, F. Grasset, E. Duguet, Magnetic nanoparticle design for medical diagnosis and therapy, J. Mater. Chem. 14 (2004) 2161–2175.
[64] R.K. Sharma, S. Dutta, S. Sharma, R. Zboril, R.S. Varma, M.B. Gawande, Fe3O4 (iron oxide)-supported nanocatalysts: synthesis, characterization and applications in coupling reactions, Green Chem. 18 (2016) 3184–3209, https://doi.org/10.1039/C6GC00864J.
[65] S.C.N. Tang, I.M.C. Lo, Magnetic nanoparticles: essential factors for sustainable environmental applications, Water Res. 47 (2013) 2613–2632, https://doi.org/10.1016/j.watres.2013.02.039.
[66] S. Ohkoshi, A. Namai, M. Yoshikiyo, K. Imoto, K. Tamazaki, K. Matsuno, O. Inoue, T. Ide, K. Masada, M. Goto, T. Goto, T. Yoshida, T. Miyazaki, Multimetal-substituted epsilon-iron oxide ε-Ga0.31Ti0.05Co0.05 Fe1.59O3 for next-generation magnetic recording tape in the big-data era, Angew. Chem. Int. Ed. 55 (2016) 1–5, https://doi.org/10.1002/anie.201604647.
[67] H. Tamura, S. Takasaki, R. Furuichi, A kinetic model of the dissolution of magnetite (Fe3O4) in EDTA solutions, Bunseki Kagaku 47 (1998) 397–403.
[68] M.A. Blesa, E.B. Borghi, A.J.G. Maroto, A.E. Regazzoni, Adsorption of EDTA and iron-EDTA complexes on magnetite and the mechanism of dissolution of magnetite by EDTA, J. Colloid Interface Sci. 98 (1984) 295–305.
[69] Critical stability constants volume 5, in: A.E. Martell, R.M.S (Eds.), Biochem. Educ. 11 (1983) 77, https://doi.org/10.1016/0307-4412(83)90054-7.
[70] A.P. Abbott, D. Boothby, G. Capper, D.L. Davies, R.K. Rasheed, Deep eutectic solvents formed between choline chloride and carboxylic Acids : versatile alternatives to ionic liquids, J. Am. Chem. Soc. 126 (2004) 9142–9147, https://doi.org/10.1021/ja048266j.
[71] S. Funahashi, Method for Producing Sintered Body, 2019. WO 2019/008711 A1.
[72] J.A. Horn, S.C. Zhang, U. Selvaraj, G.L. Messing, S. Trolier-Mckinstry, Templated grain growth of textured bismuth titanate, J. Am. Ceram. Soc. 82 (1999) 921–926.
[73] G.L. Messing, S. Trolier-McKinstry, E.M. Sabolsky, C. Duran, S. Kwon, B. Brahmaroutu, P. Park, H. Yilmaz, P.W. Rehrig, K.B. Eitel, E. Suvaci, M. Seabaugh, K.S. Oh, Templated grain growth of textured piezoelectric ceramics, Crit. Rev. Solid State Mater. Sci. 29 (2004) 45–96, https://doi.org/10.1080/10408430490490905.
[74] A. Ndayishimiye, K. Tsuji, K. Wang, S.H. Bang, C.A. Randall, Sintering mechanisms and dielectric properties of cold sintered (1-x) SiO2-x PTFE composites, J. Eur. Ceram. Soc. 39 (2019) 4743–4751, https://doi.org/10.1016/j.jeurceramsoc.2019.07.048.
[75] J.J. De Yoreo, P.U.P.A. Gilbert, N.A.J.M. Sommerdijk, R.L. Penn, S. Whitelam, D. Joester, H. Zhang, J.D. Rimer, A. Navrotsky, J.F. Banfield, A.F. Wallace, F.M. Michel, F.C. Meldrum, H. Cölfen, P.M. Dove, Crystallization by particle attachment in synthetic, biogenic, and geologic environments, Science 349 (2015) 1–8, https://doi.org/10.1126/science.aaa6760.
[76] C. Elissalde, U.-C. Chung, M. Josse, G. Goglio, M.R. Suchomel, J. Majimel, A. Weibel, F. Soubie, A. Flaureau, A. Fregeac, C. Estournès, Single-step sintering of zirconia ceramics using hydroxide precursors and Spark Plasma Sintering below 400 ° C, Scripta Mater. 168 (2019) 134–138, https://doi.org/10.1016/j.scriptamat.2019.04.037.
[77] P.W. Voorhees, The theory of Ostwald ripening, J. Stat. Phys. 38 (1985) 231–252.
[78] J. Subrt, V. Balek, J.M. Criado, L.A. Perez-Maqueda, E. Vecernikova, Characterization of α-FeOOH grinding products using simultaneous DTA and TG/DTG coupled with MS, J. Therm. Anal. 53 (1998) 509–517.
[79] X. Song, J.-F. Boily, Surface, Bulk Thermal, Dehydroxylation of FeOOH polymorphs, J. Phys. Chem. 120 (2016) 6249–6257, https://doi.org/10.1021/acs.jpca.6b04294.
[80] S. Music, A. Vertes, G.W. Simmons, I. Czako-Nagy, H. Leidheiser, Mössbauer spectroscopic study of the formation of Fe (lll) oxyhydroxides and oxides by hydrolysis of aqueous Fe (lll) salt solutions, J. Colloid Interface Sci. 85 (1982).
[81] R.J. Atkinson, A.M. Posner, J.P. Quirk, Crystal nucleation and growth in hydrolysing iron (III) chloride solutions, Clay Clay Miner. 25 (1977) 49–56.
[82] K. Toda, S.W. Kim, T. Hasegawa, M. Watanabe, T. Kaneko, A. Toda, A. Itadani, M. Sato, K. Uematsu, T. Ishigaki, J. Koide, M. Toda, Y. Kudo, T. Masaki, D.H. Yoon, Novel soft chemical synthesis methods of ceramic materials, Key Eng. Mater. 690 (2016) 268–271, https://doi.org/10.4028/www.scientific.net/KEM.690.268.
[83] K. Toda, S.W. Kim, T. Hasegawa, M. Watanabe, T. Kaneko, A. Toda, R. Yamanashi, S. Kumagai, M. Muto, A. Itadani, M. Sato, K. Uematsu, T. Ishigaki, J. Koide, M. Toda, E. Kawakami, Y. Kudo, T. Masaki, D.H. Yoon, Development of water assisted solid state reaction for the ceramic materials, Key Eng. Mater. 751 (2017) 353–357, https://doi.org/10.4028/www.scientific.net/KEM.751.353.
[84] K. Toda, T. Kaneko, T. Hasegawa, M. Watanabe, Y. Abe, T. Kuroi, M. Sato, K. Uematsu, S.W. Kim, Y. Kudo, T. Masaki, D.H. Yoon, Synthesis of nano-sized materials using novel water assisted solid state reaction method, Key Eng. Mater. 777 (2018) 163–167, https://doi.org/10.4028/www.scientific.net/KEM.777.163.
[85] T. Kozawa, K. Yanagisawa, Y. Suzuki, Water vapor-assisted solid-state reaction for the synthesis of nanocrystalline BaZrO3 powder, J. Ceram. Soc. Japan 121 (2013) 308–312.
[86] M. Watanabe, J. Inoi, S.W. Kim, T. Kaneko, A. Toda, M. Sato, K. Uematsu, K. Toda, J. Koide, M. Toda, E. Kawakami, Synthesis of Li2SiO3 using novel water-assisted solid state reaction method, J. Ceram. Soc. Japan 125 (2017) 472–475.
[87] M.M. Antonova, The preparation of low-porosity specimens of titanium and zirconium hydrides by the method of reactive sintering, Sov. Powder Metall, Met. Ceram 4 (1965) 538–544, https://doi.org/10.1007/BF00774255.
[88] F.J.C.M. Toolenaar, M.T.J. Verhees, Reactive sintering of zinc ferrite, J. Mater. Sci. 23 (1988) 856–861.
[89] D.G. Kleshchev, A.V. Tolchev, V.Y. Pervushin, Phase formation in the system FeOOH-Zn(OH)2-H2O under hydrothermal conditions, Russ. J. Appl. Chem. 76 (2003) 1384–1388, https://doi.org/10.1023/B:RJAC.0000012652.50279.0c.